



Full Text View

[Volume 31, Issue 9 \(September 2001\)](#)

Journal of Physical Oceanography

Article: pp. 2590–2611 | [Abstract](#) | [PDF \(2.29M\)](#)

North Pacific Subtropical–Tropical Gyre Exchanges in the Thermocline: Simulations with Two Isopycnic OGCMs

Victoria J. Coles

NASA Goddard Earth Sciences and Technology Center, Greenbelt, Maryland

Michele M. Rienecker

Oceans and Ice Branch, NASA Goddard Space Flight Center, Greenbelt, Maryland

(Manuscript received May 16, 2000, in final form December 14, 2000)

DOI: 10.1175/1520-0485(2001)031<2590:NPSTGE>2.0.CO;2

ABSTRACT

This study considers the advective transport in the thermocline between the subtropical and tropical Pacific using two different models: MICOM (fully isopycnal) and Poseidon (quasi-isopycnal). The annually averaged model climatologies are comparable to other model and observational results, with Poseidon showing relatively greater western boundary current exchange and MICOM having a more significant basin interior pathway. This difference is related to the different representations of the thermocline ridge associated with the ITCZ, and of the zonal current systems at 8°–10°N.

In both models, the interior exchange pathway is highly seasonal, with pulsed southward flow occurring during the fall and early winter as the thermocline thickens. This is the time period when the thermocline is shallowest in the central Pacific associated with the maximum North Equatorial Countercurrent transport and when the Ekman pumping associated with positive wind stress curl is shifted northward in the Tropics.

Idealized tracer fields show both the continuity and seasonality of the transport pathway between subtropics and the equator, with enhanced pumping of tracer into the equatorial Pacific at 140°W over a 6-month (fall/winter) period, followed by a quiescent (spring/summer) period. Both models suggest that not only is the interior flow across the potential vorticity maximum constrained to a relatively small zonal region but, also, that the shallow subtropical overturning cell is a localized process with significant zonal variation in intensity.

Table of Contents:

- [Introduction](#)
- [Model description](#)
- [Model data comparison](#)
- [Annually averaged exchange](#)
- [Seasonal exchange](#)
- [Discussion](#)
- [REFERENCES](#)
- [TABLES](#)
- [FIGURES](#)

Options:

- [Create Reference](#)
- [Email this Article](#)
- [Add to MyArchive](#)
- [Search AMS Glossary](#)

Search CrossRef for:

- [Articles Citing This Article](#)

Search Google Scholar for:

- [Victoria J. Coles](#)
- [Michele M. Rienecker](#)

1. Introduction

The question of how decadal variability in the ocean–atmosphere system influences the initiation, intensity, frequency, and predictability of ENSO and other short term climate fluctuations has received much attention recently because of evidence of interdecadal changes in the onset of El Niño (e.g., [Wang 1995](#)) and its predictability (e.g., [Balmaseda et al. 1995](#); [Chen et al. 1997](#)). The underlying cause of these variations is not yet understood; however, many investigators (e.g., [Liu and Zhang 1999](#); [Zhang et al. 1998](#); [Zhang et al. 1999](#)) have suggested that the source lies in linkages between the subtropical and tropical oceans.

Near the equator, the oceans adjust rapidly to atmospheric forcing variability due to the rapid Rossby and Kelvin wave propagation speeds. This response timescale has led to the suggestion that decadal variability in the Tropics may have its origins in the subtropics where adjustment through wave processes is slower, and advective timescales can be on the order of decades. A number of theories exist to explain the interaction and its contribution to decadal variability in the ENSO signal. The advective theories suggest that salinity, thermal, or transport anomalies generated in the subtropics influence the properties of the tropical thermocline ([Gu and Philander 1997](#); [Zhang et al. 1997](#); [Kleeman et al. 1999](#)).

This study examines the pathways, transports, and seasonal variability associated with this advective interaction in numerical models of the North Pacific Ocean. The focus of this paper is on the Northern Hemisphere exchange. Observations ([Johnson and McPhaden 1999](#)) indicate that the connection between the Southern Hemisphere subtropical gyre and the equatorial current system may be of equal or greater magnitude, and the simulations presented here clearly include those exchanges. However, whereas the pathways from the Southern Hemisphere seem straightforward, the so-called potential vorticity barrier in the Northern Hemisphere leads to questions concerning the precise pathways from the north to the equator. The advective connection between the two North Pacific gyre systems is thought to occur through a subtropical cell ([McCreary and Lu 1994](#)) in which warm surface water flows northward driven by surface wind stresses. This poleward flow is returned in the thermocline by water subducted in the subtropics. Tropical thermocline water is then upwelled at the equator to close the mass balance ([Hirst et al. 1996](#)).

Much of the Northern Hemisphere subtropical–tropical water mass exchange occurs in low-latitude western boundary currents, specifically the Mindanao Current ([Lu and McCreary 1995](#); [Wijffels et al. 1996](#)). However, observational evidence also supports a midbasin source of subtropical water to the equatorial thermocline. [Fine et al. \(1987\)](#) show an equatorial vertical section of tritium on density surfaces that has a local maximum in the thermocline at 140°W, distinct from elevated thermocline tritium concentrations nearer the western boundary. The Northern Hemisphere input function for tritium argues that the source of this fluid is the North Pacific. While this fluid may pass through the western boundary current system directly into the North Equatorial Countercurrent (NECC) and then southward to the equator, the relatively high tritium concentrations suggest a more direct link. [McPhaden and Fine \(1988\)](#) interpreted this tracer as flow in the thermocline from the subtropics to the Tropics, consistent with the Sverdrup circulation. The scarcity of direct observations for resolving the weak interior flow and its seasonal and interannual variability has led to the study of this problem primarily in the context of numerical models, with the exception of the recent study by [Johnson and McPhaden \(1999\)](#) in which a Pacific climatology based on a large hydrographic database was used to show an average interior pathway with order 5 Sv ($\text{Sv} \equiv 1 \times 10^6 \text{ m}^3 \text{ s}^{-1}$) of transport in the thermocline.

To date, the modeling studies of subtropical–tropical gyre interactions in the Pacific (e.g., [McCreary and Lu 1994](#); [Rothstein et al. 1998](#); [Liu and Huang 1999](#)) have tended to focus on annually averaged processes. This seems justified by the observational study by [Wijffels et al. \(1996\)](#), which finds the seasonal signal in dynamic height at eastern and western extremes of the Pacific basin at 10°N to be only 20% of the total variability. However, the seasonal variation of 4 Sv is half the mean flow. [McCreary and Lu \(1994\)](#) studied tracer advection in a seasonal flow field. Their study found no significant effects on the tracer fields; however, this may have been due to the very limited vertical resolution in their simulations. Here, in higher resolution GCMs, we investigate the role that the seasonal cycle plays in mediating meridional exchange between the North Pacific subtropical and tropical gyres, and in particular on the northern interior pathway, which gives rise to the observed tritium distribution.

The robustness of the result is assessed by comparison of two oceanic general circulation models; MICOM and Poseidon ([Bleck et al. 1989](#); [Schopf and Louhe 1995](#)). While both models are formulated based on density as a vertical coordinate, significant differences exist in the model implementation of the vertical coordinate, the barotropic mode, and the mixing parameterizations. Here, a fairly extensive comparison of the model fields and data is first used to validate both models' tropical and extratropical performance, including a direct comparison of the model transports with available data from the Pacific Ocean. Since the observational database inadequately resolves the seasonal cycle of even the major current systems in this region or in particular the seasonality of intergyre exchanges, the use of two different models run under almost identical configurations provides some indication that the results are a relatively general GCM response to the applied forcing and are not model specific.

In [section 2](#), the model parameters and forcing are described. In [section 3](#) the fields from both models forced by monthly climatological forcing are described and compared to remotely sensed and in situ data. In particular, comparison of modeled and observed transports on annual and seasonal timescales is made. In [section 4](#), annual meridional exchange pathways in the models are compared with other model and observational studies. The seasonality of the interior exchange and a mechanism explaining that seasonality as well as ideal tracer distributions demonstrating the continuity of the isolated meridional exchanges are shown in [section 5](#).

2. Model description

The two models used in this study are the Poseidon quasi-isopycnal model ([Schopf and Loughe 1995](#); [Yu and Schopf 1997](#)) and the Miami Isopycnal Coordinate Ocean Model (MICOM: [Bleck et al. 1989](#); [Bleck and Smith 1990](#); [Bleck et al. 1992](#)). The choice of a level or layer model often depends on the problem of interest. Here layer models are a natural coordinate choice because we are interested in the transport and pathways of integral water masses. These water masses obtain their characteristic properties through ventilation at the mixed layer base, and these properties are largely conserved, with mixing occurring primarily along isopycnal surfaces.

Vertical resolution is concentrated primarily in the tropical thermocline in order to accurately model the complex vertical current structure at the equator and this choice precludes having much resolution subthermocline in the subtropics. The primary diffusion parameters and forcing for both models are shown in [Table 1](#), and the models and external forcing are briefly described below. The forcing and configuration of the models are similar, but not exact due to differences in the models' projections and grids. Although this means the intercomparison of the model results is somewhat informal, it also means the model similarities are more robust.

MICOM (version 2.7) and Poseidon (version 4.0) consist of a stack of layers, each obeying the shallow-water equations. At the surface, [Kraus and Turner \(1967\)](#) type bulk mixed layers entrain and detrain seasonally, linking the surface fluxes of heat, salt, and momentum with the interior isopycnal and quasi-isopycnal domains. This is a simplistic representation of a slab mixed layer, which fails to represent all the complex processes occurring in the oceans through shear instabilities and internal wave dynamics; it does however produce a realistic seasonal cycle.

Momentum is not mixed diapycnally in MICOM aside from a homogenization scheme that operates only at the base of the mixed layer, amounting to a vertical mixing coefficient, in general, two orders of magnitude lower than for horizontal mixing. Isopycnal mixing is implemented through a background Laplacian diffusion augmented with a [Smagorinsky \(1963\)](#) shear-dependent coefficient. [Yu and Schopf \(1997\)](#) tested vertical mixing parameterizations extensively in Poseidon, and the model uses the Richardson-number-dependent mixing scheme of [Pacanowski and Philander \(1981\)](#). Shear-dependent mixing in Poseidon acts to strengthen the Equatorial Undercurrent (EUC) and improve its representation compared to a constant vertical viscosity. The isopycnal mixing and diffusion are implemented through an eight-order Shapiro filter ([Shapiro 1970](#)).

The model domain extends from 45°S to 64°N. The northern boundary is closed at the Aleutian archipelago and Bering Strait. The southern boundary is closed at 45°S with layer thickness, temperature, and salinity relaxed to monthly Levitus climatology values in a buffer zone near the boundary. The western boundary is closed, so there is no Indonesian Throughflow. The model resolution is 2/3° by 2/3° cos(latitude) by 20 layers on a Mercator grid in MICOM. The vertical spacing of the layers can be seen in [Figs. 3a and 3b](#); most of the resolution is concentrated within the equatorial thermocline. Poseidon uses a stretched grid with zonal spacing of 1° and meridional mesh size varying from 1/3° between 10°N and S, stretching to 1° at 20°N and S. At this resolution, western boundary currents are not well resolved in the models; however, the details of the boundary current structure at midlatitudes are less important than obtaining realistic gyre transports for this study. MICOM incorporates a barotropic mode through a split-explicit algorithm ([Smith et al. 1990](#)), and topography from the 5-min ETOPO-5 database is smoothed and interpolated to the model grid. This version of Poseidon is a reduced-gravity model with 20 active layers. In both models, land boundaries are taken according to the 200-m isobath.

The model forcing is provided by a blend of Florida State University (FSU) pseudostress ([Stricherz et al. 1992](#)) with a constant drag coefficient of 1.3×10^{-3} and National Centers for Environmental Prediction (NCEP) reanalysis surface stress outside the 30°N and S meridians. Surface freshwater flux is provided by climatological Xie–Arkin precipitation ([Xie and Arkin 1996](#)). Surface heat flux is provided through the bulk atmospheric boundary layer model of [Seager et al. \(1995\)](#), with flux components estimated from the datasets shown in [Table 1](#).

MICOM and Poseidon are integrated for 15 years from an initial thermohaline state set by the Levitus climatology, with the climatological forcing described above. A longer experiment with a 30-year Poseidon run shows no significant change in the subtropical–tropical exchange process described below, suggesting that the dominant processes influencing the exchange process are adequately spun up in the 15-year simulations.

3. Model data comparison

Characterization of the intergyre transport requires realistic gyre and thermohaline circulations both in the interior and at depth, so the models are first validated against observations. Most direct estimates of current speed and transport have concentrated on the western boundary regions where the flows are sufficiently large to be monitored over relatively short time periods. For this reason, although the focus here is on understanding midbasin intergyre exchange, model performance is validated primarily at the surface, and in the western boundary regime.

Mixed layer velocity and sea surface height (SSH) fields for the last September of the climatological runs are shown in [Figs. 1a and 1b](#). For comparison of both the mean and the structure of the mesoscale fields, the mean September 1996 SSH anomaly field from TOPEX altimeter data is shown in [Fig. 1c](#). Since the TOPEX data are anomalies only, the mean field for [Fig. 1c](#) is obtained from the Levitus climatological dynamic height relative to 2000 dbar. The Levitus climatology may be expected to underestimate the SSH maxima and minima associated with tropical and equatorial currents due to the broad spatial smoothing (order 500 km). However, since neither model yields perfectly analogous fields to the SSH derived from hydrographic measurements, the comparison should be qualitative rather than quantitative. In the Poseidon model, SSH is represented by the dynamic height field relative to 2200 m.

The basic circulation features associated with the North and South Pacific subpolar and subtropical gyres and the surface tropical and equatorial currents can be seen in both models. MICOM and Poseidon show a dual-lobed subtropical gyre structure that extends across the Pacific basin ([Figs. 1a and 1b](#)), capturing the subtropical countercurrent near 20°N. The tight recirculation of the Kuroshio is 5°–10° too far south in Poseidon. The observations show only a hint of the dual-lobed subtropical gyre structure in the western basin, with the southern limb dominant ([Fig. 1c](#)). The nature of the climatology, which averages over all seasons and a number of years, will tend to obscure features whose position varies over time.

[Table 2](#) shows annual average volume transports of major tropical and equatorial current systems for each model and the available observations. The definition of the region used in computing the observed transports has been kept as close as possible to that used in the observational studies. No attempt is made to interpolate the model onto a finer vertical resolution; if a density layer misses one of the criteria, its transport is excluded.


Both models show North Equatorial Currents (NEC) of the same magnitude forming the westward return flow for the subtropical and tropical gyres. In MICOM, the NEC has a poleward component in the central basin that may be supplying water for the eastward flow associated with the southern limb of the subtropical gyre (subtropical countercurrent). Poseidon also has a slight northward component to the NEC in the central Pacific, but the magnitude is smaller. Poseidon and MICOM have similar transports that tend to underestimate both the NECC and the NEC relative to the [Wyrтки and Kilonsky \(1984\)](#) observational estimates, which are based on the thermal wind equations and a level of no motion at 1000 m. This study uses a large number of CTD casts that resolve the seasonal cycle quite well. [Donguy and Meyers \(1996\)](#) find an annual average transport of 14 Sv, which is lower than the simulated averages, thus interannual variability may influence the average estimate. The NEC and NECC are associated with the pronounced trough centered at 10°N in the SSH fields of both models and observations. This structure extends down through the thermocline and constitutes a significant barrier to meridional interior exchange between the North Pacific subtropical and tropical gyres.



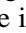
MICOM shows stronger westward equatorial surface velocities in general than Poseidon (90–100 cm s⁻¹ vs 70 cm s⁻¹) (see [Figs. 1 and 2](#)) and somewhat higher velocities than the drifter-based observations ([Reverdin et al. 1994](#)). However, the transports of both models are in line with observations (see [Table 2](#)). Spatially, both models have strong westward mixed layer flow in September at the equator in the South Equatorial Current (SEC), consistent with both TAO current meter mooring observations (e.g., [Yu and McPhaden 1999](#)) and the drifting buoy climatology of [Reverdin et al. \(1994\)](#). Equatorial divergence is obvious, and the associated upwelling forms the SSH trough on the equator in both models and observations.


Because the exchange of mass and material properties from the subtropical to tropical gyres occurs within the density range associated with the thermocline, a reasonable representation of the ventilation of the subtropical thermocline is important to resolving exchange processes. Models must then correctly simulate maximum winter mixed layer depths and densities as well as the detrainment and mixing processes in order to appropriately ventilate the correct density range. While a study of ventilation processes is beyond the scope of this work, maximum mixed layer depths generally occur in March in the Northern Hemisphere subtropical gyre, and the modeled and observed SSTs tend to have a local minimum simultaneously. The March sea surface temperature (SST) from a climatology constructed by [Casey and Cornillon \(1999\)](#) is shown in [Fig. 2c](#) for comparison with the modeled mixed layer temperatures ([Figs. 2a and 2b](#)). Both models show warm subpolar mixed layers. This may be due both to limitations of the atmospheric mixed layer model, which determines the turbulent components of the net heat flux, and to imbalances between freshwater forcing and evaporative fluxes. [Yang et al. \(1999\)](#), for example, show that differences in precipitation estimates can lead to temperature differences of up to 1°C in modeled SST. In both models, the subpolar region also warms through transport of subtropical warm water into the subpolar region by the Kuroshio, which separates north of the observed separation point. This is expected in models with insufficient resolution in the boundary layer. The warming is partly offset in the MICOM simulation by excess surface


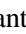
salinity, which explains the differences in surface expression of the 24.5–26.2 σ_θ thermocline layer. While the associated geostrophic currents may be impacted by these density anomalies, the simulations are not of sufficient duration for subpolar processes to influence the exchange pathways discussed here.

In the subtropical regime, both models represent the wintertime mixed layer temperatures well. The meridional temperature gradient is reduced, in general, by the warm subpolar regions, but in the region between 10°N and 20°N the models are very close to observations. Further south, between 20°S and 10°N, the models reproduce the structure of the meridional temperature gradients; however, the absolute SSTs differ somewhat. MICOM is too warm in the western warm pool. While atmosphere–ocean feedbacks tend to prevent the ocean from warming beyond 30°C in the observations, MICOM has isolated regions reaching 32°C. In contrast, Poseidon has maximum warm pool temperatures less than 29°C and tends to be 1° to 2°C too cool over the whole equatorial region. The shaded mixed layer density suggests regions in which the thermocline may be in contact with the mixed layer through entrainment (in the subtropics) or detrainment (near the equator).

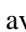
The zonal velocity field for both models and the averaged observations of [Wyrki and Kilonsky \(1984\)](#) are compared in a meridional section at 155°W ([Fig. 3](#) ). The structure of the NEC with deeper extensions to the north is captured in both models. The hydrographic measurements suggest a subsurface maximum in the NECC, which is observed as a weak sub-mixed layer maximum in the Poseidon simulation. Neither model has equatorial undercurrent (EUC) velocities as high as the observations would suggest (100 cm s⁻¹); however, instantaneously both models do attain such speeds. The spatial structures of the EUC and the North and the South Equatorial Countercurrent are quite well resolved in both models.

The observed zonal variability in thickness and depth of the thermocline is represented in both models. The thermocline is decomposed into three layers according to density: $\sigma_\theta = 22.0\text{--}23.0$, 23.0–24.5, and 24.5–26.2. These layers, shaded in [Fig. 3](#)  and whose wintertime surface expression is shown in [Fig. 2](#) , will be discussed further in [section 5](#). The thermocline is thick in the south, then shoals and thins toward the equator where it broadens again, associated with equatorial upwelling and downwelling. To the north, in the NECC and NEC, the thermocline shoals, thins, and then deepens again sharply. This thermocline ridge is the subsurface signature of the SSH trough seen in [Fig. 1](#)  and is associated with very high values of potential vorticity (e.g., [Talley 1988](#)). Because Poseidon is quasi-isopycnic, the density of layers may vary near regions where layer thickness is small. As a result, the signature of the thermocline is seen more in the temperature than layer structure.

The vertical structure of the salinity field ([Fig. 3](#) , lowest panels) in both models is comparable to observations, although both models tend to overestimate the salinity in the subtropical thermocline waters. This is due to excessively saline subpolar and northern subtropical gyre surface conditions in both models. The evaporation and precipitation forcings are independent, so the freshwater flux over the Pacific Ocean is not balanced. In particular, the surface salinity fronts associated with the subtropical gyres in both hemispheres are equatorward of the observations. However, both models show a reasonable equatorward penetration of the subtropical salinity maxima in the thermocline and the deeper Northern Hemisphere salinity minimum.

The importance of resolving the seasonal cycle can be seen in the strong seasonal cycling of the transports of the major zonal currents across 155°W ([Fig. 4](#) ). The last two model years are shown to suggest the degree of interannual variability inherent in the nonlinear system even without interannual variability in the external forcing. The transports differ only slightly between the years. Both simulations show the maximum eastward EUC transport out of phase with maximum eastward transport in the NECC and in phase with minimum westward transport in the SEC. In both models, the EUC and SEC show a distinct semiannual cycle, although the amplitude of the semiannual period mode differs between the models. The models have SEC maxima in the same month, but a 1 month phase lag with MICOM leading Poseidon in the SEC minima. This lag is duplicated in the EUC maxima. Because the equatorial currents are so strongly wind driven, the lag in the SEC minimum, which is vertically coherent with the EUC, is surprising. In the equatorially confined currents in particular, MICOM has greater peak to peak annual and semiannual variability. This may be tied to differences in the diapycnal mixing; MICOM has no diapycnal momentum mixing, whereas Poseidon uses a Pacanowski–Philander Richardson number dependence as described in [Yu and Schopf \(1997\)](#), which tends to be preferentially expressed in the equatorial band where vertical shear is large. At 155°W, the zonal component of the surface wind stress has a weak semiannual signal (e.g., [Yu and McPhaden 1999](#)) but the dominant periodicity is annual. [Table 3](#)  lists a comparison of the maximum and minimum equatorial current transports compared with a few observational estimates. The models are relatively consistent with the timing of the observations, suggesting that the seasonal signal of their wind-driven transport is realistic, even if the absolute magnitudes differ as a result of model and forcing error and interannual variability in the observations. In general, the large transport variations of the simulated equatorial currents in particular suggest that individual estimates of transport based on a single ship track must be compared with observations and models from the same season if not year.

4. Annually averaged exchange

Zonal vertical sections of the 3-yr average of meridional volume transport across 10°N are shown in [Fig. 5](#) . In any

one year, the structure of the meridional transport is banded due to westward propagating Rossby waves. Even in the 3-yr averages shown however, the banding is persistent in some regions in and below the pycnocline. Within the mixed layer, transport is northward across most of the Pacific except in the far eastern basin. All the model sections between 10° and 6° N show southward flow in the mixed layer east of 130°W.

Subsurface, the pycnocline shoals and thins to the east in both models due to the influence of the ITCZ (Lu and McCreary 1995) and in accord with observations. There is little southward transport in the compressed pycnocline. The potential vorticity maximum associated with the upwelled pycnocline creates a meridional gradient in potential vorticity that inhibits meridional flow. To the west, as the thermocline opens (near 160°W in the averaged sections), the potential vorticity gradient weakens, the barrier to exchange is relaxed, and transport in the thermocline is to the south.

In both models, this region of increased meridional transport lies between roughly 160°E and 160°W. This is a region of interior meridional exchange between the subtropical and tropical gyres. Similar interior transport (though perhaps not as far to the west) has been observed previously in numerical models (Rothstein et al. 1998; Huang and Liu 1999), and appears to be a robust feature of the observed flow as well (Johnson and McPhaden 1999).

In Table 4, the annually averaged transport within density layers that correspond to those of other observational and modeling studies are shown for comparison. The layers delineated earlier ($\sigma_\theta = 22.0\text{--}23.0$, $23.0\text{--}24.5$, $24.5\text{--}26.2$ kg m⁻³ are upper-, mid-, and lower-thermocline layers, respectively) are shaded in Fig. 3, so their relation to both the water mass properties and dynamical flow regimes can be seen. The layers are somewhat arbitrary with respect to the model dynamics; however, they provide useful guidelines in the model–data comparison. The upper-thermocline layer corresponds roughly to the seasonal thermocline, which is poorly represented in the annual average, as it has a finite vertical expression over only part of the year. The midthermocline layer corresponds to the upper portion of the EUC and the more frequently ventilated upper permanent thermocline. The high salinity subtropical water is mostly contained in the lower permanent thermocline layer.

At 8°N, the analysis of a large hydrographic dataset (Johnson and McPhaden 1999) shows a total southward interior transport of 5 Sv in the basin interior, with that transport concentrated more in the upper and mid thermocline. The model of Huang and Liu (1999) follows closely these observations, with slightly lower transport in the upper thermocline. Poseidon underestimates the interior thermocline transport by 0.5 Sv, and MICOM overestimates the transport by 3.5 Sv. This discrepancy is also apparent at 10°N, where Poseidon underestimates the transport by 2.5 Sv and MICOM overestimates by 0.5 Sv relative to Huang and Liu (1999). Poseidon and MICOM both disagree with Huang and Liu (1999) on the direction of transport in the lower thermocline.

Comparison of the modeled and observed western boundary current transports in Table 4 immediately suggests the importance of the definition of the western boundary current regime. Here we have chosen to be consistent with the prior studies in using the preselected invariant longitudinal range for the boundary current. Depending on the properties of the boundary current recirculation, small changes in the boundary current width greatly influence the results. At 10°N in the western boundary current, for example, Poseidon has 3 Sv more transport than the observations would suggest, and MICOM has 4–5 Sv fewer. This nearly compensates for the interior discrepancy.

The two models used in this study have the same net transport between the subtropical and tropical gyres when averaged zonally across the basin. In contrast, the partitioning between the western boundary current and interior pathways is more dependent on the specifics of the model dynamics, and their integrated response to local surface forcing. The simulated transports are consistent with the observational estimates shown, which suggests that absence of an Indonesian Throughflow is not a significant liability.

5. Seasonal exchange

Previous studies of tropical–subtropical exchange used annually averaged observations or model flow fields to advect Lagrangian particles in the thermocline or compute meridional transports. However, the strong seasonality of the zonal NECC and the Ekman pumping suggests that the potential vorticity signal associated with the current may also be correspondingly stronger or weaker on a seasonal basis. Lu and McCreary (1995) dismissed the importance of the annual cycle in mediating meridional exchange based on the similarities of the mean flow and tracer fields in runs that were forced with annual and seasonally varying winds. Their simulations used a model with very limited vertical resolution (2½ layers). While the process described in the following section should operate at low resolution, it is possible that their thermocline layer is never shallow or thin enough to be significantly impacted by Ekman pumping. They point out that all of the geostrophic transport in their model is carried in the uppermost layer. In these models, a significant fraction of the geostrophic transport is carried in the thermocline, and this is the component that is exchanged between gyres.

Here, the meridional volume transport is summed at 8°N, and the corresponding layer thickness averaged zonally from 160°E eastward to the boundary. This criterion is based on the region in the model in which southward flow across the

ITCZ penetrates all the way to the equator (see [Figs. 10 and 11](#)). In [Fig. 6](#), the interior volume transport within each layer is shown over the zonal average of layer thickness to suggest the vertical structure of the transport profile. The maximum in potential vorticity, which reflects the blockage of meridional flow, is centered near 8°N in both models. While the models resolve the magnitude of the exchange processes somewhat differently, some similarities are immediately apparent.

The mixed layer has strong northward wind-driven Ekman flow throughout most of the year at these latitudes. The seasonality in both models is consistent with the wind forcing: strong forcing in winter when the mixed layer is deepening and weak in summer as the mixed layer shoals. Below the mixed layer, the exchange can be partitioned into layers within the thermocline as discussed above.

The seasonal thermocline ($22\text{--}23 \sigma_\theta$) is ventilated in boreal spring when the mixed layer reaches its maximum depth in both models at 8°N ([Fig. 6](#)). In late summer and fall, this fluid is subducted (or injected) as the mixed layer detrains or shoals, leaving behind fairly unstratified fluid in the seasonal thermocline. This ventilation is accompanied by strong southward flow within these layers (the upper thermocline in our decomposition) and a reduction in the mixed layer poleward Ekman flow as the wind field relaxes. The seasonal thermocline layers are of course only permanently subducted when they reach latitudes at which the wintertime mixed layer depth is shallower than the depth of the previously injected layers.

Deeper, the permanent thermocline (mid- and lower-thermocline layers discussed earlier) has a somewhat different seasonality. More fluid is transported meridionally to the tropical gyre in these layers during fall as the mixed layer begins to deepen. At this time the zonal average lower thermocline is still upwelling. In the lower permanent thermocline, there is a semiannual signal in both models, particularly in Poseidon. Although the timing of the southward transport early in the year is slightly different, the transition from southward to northward transport in each model occurs at the time of deepest mixed layer when the thermocline is tightly compressed.

a. Interior exchange

While a possible interior pathway for thermocline exchange between the subtropical and tropical gyres has been recognized from tracer measurements and model simulations ([Fine et al. 1987](#); [McPhaden and Fine 1988](#); [Lu et al. 1998](#)), the details of the transport are poorly understood. [McPhaden and Fine \(1988\)](#), among others, showed that the geostrophic wind-driven flow in the interior of the Pacific basin is southward and could result in a circuitous pathway for exchange from the NEC to the NECC, finally convergent onto the equator. However, the compression of the thermocline at 10°N, seen in meridional sections of water mass properties ([Fig. 3](#)), the surface height fields ([Fig. 1](#)), and in submixed layer maps of potential vorticity ([Talley 1988](#)), has been thought to block any prospective interior pathway. This potential vorticity maximum is created by the wind stress curl-forced thermocline tilt associated with the zonal NEC and NECC flows. The SSH distribution ([Fig. 1](#)) suggests that to the west this front weakens, and some midbasin exchange has been noted in other numerical modeling studies ([Rothstein et al. 1998](#); [Liu and Huang 1998](#); [Huang and Liu 1999](#)).

In [Figs. 7 and 8](#), the simulated meridional transport within the interior pathway band (170°E–130°W) vertically integrated over the upper and middle through lower thermoclines is shown as a function of time at 8°N. This region is chosen based on the accumulation of meridional transport from the eastern boundary (not shown). West of a narrow poleward flowing eastern boundary current centered at 100°W, there is no significant meridional flow until 160°W. Although southward flow across 8°N occurs west of 170°W, the seasonality of the flow differs from the central basin, and little of this flow appears to continue southward to the equator (see [Fig. 11](#)). [Figure 7](#) integrates the transport between the 22.0 and 23.0 σ_θ interfaces for the two model runs. The upper panel shows the thickness anomaly (based on an annual average) between the two density interfaces.

In the interior, there is a pronounced seasonal cycle in the meridional transport within the seasonal thermocline, coherent with thermocline thickness anomalies. Virtually all of the meridional transport associated with the basin interior occurs over a 5-month window between June and November. Annual mean southward transport ranges from 0.3 to 0.8 Sv for Poseidon and MICOM, respectively. However, 85% of the total annual volume transport occurs in 3 months (2.5 Sv in the 3-month average) when the thermocline is thicker than its annual average in MICOM. For Poseidon, 70% (1 Sv in the 3-month average) of the transport occurs in three months. This is the time period in which the mixed layer shoals or detrains, inflating or thickening the seasonal thermocline, and correspondingly decreasing the local potential vorticity within the inflated layers. Poseidon shows a 1–2 month offset associated with maxima in thermocline thickness anomaly, which is consistent with the phase of other equatorial transport anomalies in this model.

The permanent thermocline [which comprises the two lower layers of [Johnson and McPhaden \(1999\)](#)] transport and thickness are shown in [Fig. 8](#). Here, the seasonal meridional transport is strongly modulated by semiannual Rossby wave propagation, particularly in Poseidon. The net southward transport is tightly coupled, however, to the positive or thick thermocline anomalies. The seasonal cycle of the thermocline thickness variability is similar in the two models, however

MICOM carries a greater net southward transport in the interior, whereas Poseidon has a greater southward transport in the western boundary current. Although the semiannual signal is stronger in Poseidon than MICOM, the net southward transport is dominated by the annual cycle in both, with excess southward transport in the late summer through winter. The models have similar phasing, although MICOM leads Poseidon by about one month, consistent with previous transports shown. Mean interior southward transport ranges from 1.7 Sv in Poseidon to 4.9 Sv in MICOM. In MICOM, 70% (6.3 Sv in the 6-month average) of the total annual transport occurs in six months, compared with 67% (2.5 Sv in the 6-month average) in Poseidon. The maximum thickness and transport periods correspond to the period when the upward Ekman pumping (suction) is maximum in the wind climatology. Poseidon shows less peak to peak variability in both thickness anomaly and transport than MICOM. This might be expected based on the lower average interior transport and lower seasonal variability in mixed layer thickness in Poseidon.

The mechanism proposed here for the existence and seasonality of the interior pathway is simply seasonal variation in the thickness of the thermocline, and thus in the magnitude and westward extent of the potential vorticity maximum. Studies of the seasonal variability in the wind stress curl and Ekman pumping at 10°N (e.g., [Kessler 1990](#)) suggest that the annual cycle in the wind-forced Ekman pumping is fairly large. Maximum Ekman pumping (suction) is associated with uplifting of the upper permanent thermocline and is consistent in phase with the seasonal cycling of the depth of the 20°C isotherm ([Kessler 1990](#)). The thermocline depth cycle has the correct general phase with respect to Ekman pumping, but the lag is affected by wave propagation contaminating the average, by the breadth of the positive Ekman pumping signal, and by the tilt of the Ekman velocity isopleths. This lag varies between one and two months for MICOM and two and three months in Poseidon, roughly consistent with the observations described by [Wang et al. \(2000\)](#). Variations in thermocline thickness associated with the enhanced meridional transport are due to these seasonal changes in wind stress curl and the annual cycle in surface wind and buoyancy forcing, which regulate the depth of the mixed layer. As Ekman pumping relaxes, the mixed layer deepens, further compressing the thermocline and restricting southward flow in the thermocline between the subtropical and tropical gyres.

The primary physical difference between the models in this region is the thickness and depth of the thermocline, which is very thin and shallow in the east, almost truncated, in MICOM, and slightly deeper and more diffuse in Poseidon. Observations of the depth of the 20°C isotherm compared with a simple quasigeostrophic model suggest that the annual cycle in wind stress pumping dominates thermocline depth variations at 10°N but that Rossby wave dynamics dominate away from the high potential vorticity regime ([Kessler 1990](#)). The thicker, deeper thermocline and slightly more northerly potential vorticity maximum may explain why the Poseidon simulation is more dominated by Rossby wave signatures than MICOM. This deficiency has been noted in other model simulations ([Donguy and Meyers 1996](#)).

The timing of the lower thermocline thickening is related to the seasonal cycle in Ekman pumping and mixed layer depth. Ekman pumping in the center of the Pacific causes upwelling of the thermocline in late summer through fall as the ITCZ moves northward and intensifies. The NECC also intensifies in response to the wind stress curl (see [Fig. 4](#) ●), and as a result, the meridional thermocline ridge is at its shallowest. The intensification of the ITCZ brings with it enhanced freshwater flux, and the mixed layer shoals due to the low turbulent mixing and stabilizing buoyancy flux. The upper thermocline upwells to the base of the (shallow) mixed layer, and this excursion is greater than the movement of the base of the thermocline leading to the thickening of the thermocline. In a fully isopycnal model away from the western boundary, only layers in contact with the mixed layer may gain or lose potential vorticity. Here, although the permanent thermocline is not ventilated in the tropical gyre, the thermocline becomes sufficiently thin that diffusive processes mixing seasonal thermocline water into the permanent thermocline may be a significant source of low potential vorticity. In spring months, the thermocline deepens concurrent with the southward movement and relaxation of Ekman pumping in the ITCZ. The NECC transport is also reduced, and the mixed layer deepens to more than 100 m, compressing the thermocline from above. The cycle of Ekman pumping over the annual cycle can be seen in [Fig. 9](#) ●, with the maximum Ekman pumping and eastward extension of upwelling favorable winds occurring in the central Pacific (1–2 months) prior to the maximum thickness anomaly in both models and observations.


The thickness anomaly of the modeled and observed permanent thermocline over time and longitude are also shown in [Fig. 9](#) ●. Although there are current meter data from the TAO array mooring at 8°N ([McPhaden et al. 1998](#)), the time series is too patchy to allow for the formation of a reasonable climatology of the meridional velocity. Here, we have constructed a temperature climatology based on TAO thermistor data from 7°N, 8°N, and 9°N. The data are averaged into a monthly climatology and interpolated onto temperature levels that reflect the spirit of the upper and lower thermocline density layers. A minimum mixed layer depth of 50 m is assumed to arbitrarily act as the upper bound of the thermocline where the upper isotherm is not defined. To compare with the TAO data, the thickness anomaly of the permanent thermocline shown in [Fig. 9](#) ● is chosen as the thickness between the 24° and 13°C isotherms minus an annual average at each longitude. The modeled pycnocline anomaly (not shown) has a similar spatial pattern to the thermocline thickness anomaly, but the magnitude of the annual cycle is stronger by 10–15 m. Clearly, the annual cycle in surface freshwater forcing and/or seasonal variability in freshwater advection influences the definition of the pycnocline.

The phase, magnitude, and longitudinal structure of the thickness anomaly from both models are consistent with observations in the permanent thermocline. The models and observations show a thicker thermocline during fall/winter in the


central basin. This time period corresponds to the timing of the increase in southward meridional transport in the basin interior. As expected, the Poseidon simulation shows greater mesoscale structure commensurate with more Rossby wave signal as compared with MICOM, but this difference is small. The thickness anomaly has a westward propagation of roughly 50 cm s^{-1} in the central Pacific, consistent with [Kessler \(1990\)](#). That both models show more mesoscale variability than the TAO data is related to the limited spatial sampling of the observations. The in situ data, which show annual variability in the thickness of the thermocline over the time period predicted by the models, provides some support for the mechanism proposed here.

b. Ventilation tracer transport

Here we have focused on the transport across the region from 8° to 10°N where the thermocline potential vorticity is at a maximum. Observational evidence for the interior pathway, however, hinges upon the continuity of the advection pathway within the thermocline and away from the western boundary current system ([Fine et al. 1987](#)). [Gu and Philander \(1997\)](#) and [Huang and Liu \(1999\)](#) among others showed the continuity of this pathway in the annually averaged numerical model flow fields. Here we verify that the southward transport described here is continuous, leading to water mass transfer between the gyres and into the equatorial undercurrent. To mimic the conditions that a water mass anomaly would experience as it flows from the subtropics to the Tropics, tracer is injected poleward of 10° in the Northern and Southern Hemispheres in the MICOM simulation. The idealized tracer tags the transfer of mass between the mixed layer and thermocline, thus the concentration of the tracer reflects the proportion of the layer ventilated in the subtropical gyre after the onset of the tracer experiment. The mixed layer concentration of tracer is arbitrarily set to 1 poleward of 10° latitude, and 0 equatorward of 10° latitude. Any water reentrained into the mixed layer immediately reacquires the surface boundary condition value. A tracer concentration of 1 reflects a layer that has been completely ventilated with mixed layer water since the onset of the tracer experiment.

[Figure 10](#)  shows the layer 10 ($\sigma_\theta = 25.0$) concentration of tracer, or the proportion of water that has been in contact with the mixed layer, in February of the third winter since tracer release. The tracer is shaded and draped over the surface representing the depth of layer 10. The thickness of this layer is contoured below. The depth surface shows the three-dimensional structure of the pathway between the subtropics and the Tropics. In the subtropics where this layer is ventilated, and has the highest tracer concentrations, the layer gradually slopes upward from west to east consistent with the Sverdrup flow in the subtropical gyre. Although the tracer is ventilated over the whole subtropical region, the sea surface height streamlines and the tracer values suggest that the interior exchange pathway must contain water that has been ventilated in the southeastern Pacific. The ITCZ thermocline ridge separates high subtropical tracer concentrations from the low tropical values. In the center of the basin, the tracer can be seen to cross the ITCZ ridge and to advect eastward and equatorward. This ridge is also a relative meridional minimum in layer thickness or maximum in potential vorticity, with tracer advection southward occurring only where the layer thickness is at least 10 m. At the equator, the depth of the thermocline slopes upward to the east, with the eastward flow in the EUC. Where upwelling into the mixed layer occurs, east of 135°W , the layer thickness gradually decreases from 20 m to nearly 0 m.

In the western basin, the tracer is seen to flow southward from the NEC in the western boundary current toward the equator. An eastward extension of the tracer core in the region of the NECC suggests that some subtropical thermocline water may reach the equator in the basin interior after having passed through the western boundary current as well. This exchange occurs on longer timescales than the direct interior exchange. Clearly the most rapid injection of North Pacific subtropical water in this simulation occurs through the basin interior. In the south, the inflow of Southern Hemisphere water in a much broader zonal band, and with relatively higher tracer concentration, is evident from 170°E to 100°W .

Maps of the tracer concentration within this layer ($\sigma_\theta = 25 \text{ kg m}^{-3}$) over time are shown in [Fig. 11](#) . Seasonal variability in the layer thickness impacts the analysis of the tracer concentration. To highlight this variability, the layer is shaded gray where it is thicker than 5 m.

The tracer is released in the fall, and the first panel (February of year 1) shows the tracer distribution in the following winter. Tracer has already reached into the tropical gyre interior, with maximum concentrations of 0.3 at 10°N . In the next six months (August of year 1), the potential vorticity maximum is strong (i.e., the layer is thinner along 10°N) and, although the 0.1 tracer contour shows that the tracer has been advected laterally in the NECC, there is little meridional transfer.

Between August of year 1 and February of year 2, however, the barrier is reduced, and a direct connection between the subtropical gyre and the NECC is seen in the 0.3 tracer contour. Furthermore, similar meridional pumping is seen between the NECC and the equatorial circulation east of 150°W , where tracer penetrates to the equator. Although the focus of this study is on the Northern Hemisphere, it is interesting to note that the connection between the southern subtropical gyre and the equatorial gyre is more rapid, and farther to the east, than the northern interior pathway. This flow is blocked at the equator, with little suggestion of cross-equatorial flow in the thermocline.

Between the second year's winter (February of year 2) and summer (August of year 2), the potential vorticity is increased again, and little meridional flow occurs. In the fall and winter (August of year 2 to February of year 3), the layer thickens again, tracer concentrations of 0.5 cross 10°N, and the 0.3 contour reaches the equator. This is the region where observations show elevated tritium concentrations ([Fine et al. 1987](#)). Although tracer concentrations in the simulation are high through much of the NECC, there is no connection between the NECC and the EUC, except in this localized band. This suggests that inflow within the thermocline to the EUC in the equatorially confined meridional overturning cell may be a localized process. It is only in this third year that tracer arrives in the equatorial circulation from the western boundary current.

The annually averaged meridional velocity for this thermocline layer ($\sigma_\theta = 25.0$) and a layer with similar density for the Poseidon model are shown in [Fig. 12](#). Meridional inflow to the EUC is concentrated in the region between 160°W and 120°W in both models, and in both hemispheres, although the MICOM model predicts a maximum inflow that is larger (up to 4 cm s⁻¹) than the Poseidon maximum (2 cm s⁻¹). This inflow corresponds to the region where tracer observations suggest that subtropical–tropical exchange occurs and to the region where [Weisberg and Qiao \(2000\)](#) show equatorial convergence in the thermocline from current meter measurements. It should be pointed out that another process that occurs preferentially in the fall season, associated with generally large NECC and SEC transports, is the formation of tropical instability waves (e.g., [Baturin and Niiler 1997](#); [Legeckis 1977](#)). It is possible that these waves influence the interior transport pathway, although it seems more likely that they are a response to the same seasonal patterns in surface wind forcing and that any influence may be through enhanced lateral dispersion of tracer and water mass properties. Superimposed on [Fig. 12](#) are the vector currents within this lower thermocline layer. The region of maximum inflow at depth corresponds to the region where surface divergence is large in the models and is just to the west of the region where the EUC bifurcates. The eastward flow continues off the equator to the North and South, and the equatorial flow reverses. The model results suggest that the subtropical and equatorial overturning cells are zonally inhomogeneous, with most of the exchange occurring on the western boundary and in the central basin where the surface divergence is large before the deep EUC reverses sign. This central basin region may be particularly susceptible to the influence of subtropical climate variability.

6. Discussion

In the mechanism advanced above, southward flow in the thermocline is impeded/inhibited in the interior by a potential vorticity ridge that acts to funnel geostrophic flow toward the western boundary. This ridge is created by upwelling of the thermocline driven by Ekman pumping and divergence and the juxtaposition of the NEC and NECC at the surface. [Wang et al. \(2000\)](#) show that this region has a local minimum in the annual range of the depth of the thermocline and that, as in [Kessler \(1990\)](#), the dynamics are slightly different from the neighboring regions on either side of the ridge. However, as shown above, because the winds vary seasonally, the thermocline depth and thickness (i.e., the intensity of the “potential vorticity barrier”) relaxes seasonally as well. The seasonal thermocline has southward transport associated with detrainment from the mixed layer in late summer and fall as the mixed layer stratifies. In fall and winter, the wind stress curl in the central Pacific at 8°N is intensified, the mixed layer is shallow, and the upper layers of the permanent thermocline are upwelled more strongly than the base. This thickens the thermocline or reduces the potential vorticity, and meridional flow within the thermocline transfers mass and water mass properties between the subtropical and tropical gyres. Interestingly, although the opening of the permanent thermocline is associated with upward Ekman pumping, the transport is equatorward rather than poleward as one would expect from the Sverdrup balance. In spring and summer, the mixed layer deepens, the wind stress curl is reduced, and the thermocline is deepened and compressed. This is the period in the models with low interior basin meridional transfer between gyres. This mechanism occurs in tandem with the intensification of the NECC and with seasonal variations in wind stress curl. The NECC has a maximum in eastward transport during the fall and winter months, which is also the time period over which the models predict interior southward transport. However, since the NECC is not in complete Sverdrup balance ([White 1974](#); [Meyers 1980](#)), other processes are likely to contribute to this variation.

This process of thermocline spreading occurs in two different layer models, one isopycnal and one quasi-isopycnal. While the use of two similar models might be considered redundant, the differences between the models are of interest, and the similarities help to confirm a process for which there are no direct observations. The exchange is more significant in the fully isopycnal model, MICOM, where the thermocline is very thin and closer to the surface in the east at 8°–10°N, than in the quasi-isopycnal model Poseidon, which has a more diffuse and deeper thermocline. Based on thermal observations, [Kessler \(1990\)](#) showed that Rossby wave activity dominated the thermocline away from 10°N, but that seasonal variations in local Ekman pumping controlled thermocline depth at the potential vorticity maximum itself. The differences between the models may be attributed to variations in mean thermocline thickness with thinner, shallower thermoclines being more responsive to seasonal variations in Ekman pumping. This is consistent with experiments using very low vertical resolution models ([Lu and McCreary 1995](#); [Liu and Huang 1998](#)), which showed that the interior pathway's existence depends on the thickness of the thermocline layer at the eastern boundary. [Lu and McCreary \(1995\)](#) attribute this to the dependence of the Ekman pumping mechanism on the thickness of the thermocline layer. The models also tend to differ in their representation of the NECC transport, with MICOM having greater transport, perhaps again tied to the representation of the thermocline at 8°N. The models show some differences in the vertical structure of the meridional flow that may reflect the differences in

their response to surface divergence, as can be seen in [Figs. 5 and 6](#). The differences may also be partly due to slight displacements in the latitudinal position of the thermocline ridge. No attempt has been made to optimize agreement between the models.

While the existence of an interior pathway has been shown previously in observations and in numerical model simulations, the inferred impact on the equatorial circulation was limited, based on the weak heat content associated with the intrusion. Both models used in this study suggest however that the interior flow across the potential vorticity maximum is constrained to a relatively small zonal region and that the entire pathway and transport are controlled by the surface wind stress curl associated with the ITCZ. Further, the equatorially constrained overturning cell is also a local process. Thus, the injection of subtropical water occurs over a relatively limited area and during a short time span, and may have a more significant impact on the equatorial thermocline than the annually averaged net meridional heat flux might suggest.

Several theories link subtropical–tropical interaction to decadal variations in ENSO activity. This mechanism suggests a means through which atmospheric midlatitude anomalies may influence the equatorial thermocline. Here the seasonality of the pathway, the strength of the exchange, and its relation to the seasonal cycle of forcing have been documented. It might be expected that similar processes will be active on interannual timescales. For example, intense winter mixing in midlatitudes might tend to create cool and anomalously thick thermocline conditions in the subtropical gyre. Under this scenario, the thickness anomaly would tend to increase interior meridional exchange between the subtropical and tropical gyres as it propagated southwestward. Furthermore, if a thermal anomaly is also associated with the thickness anomaly, then the net heat flux to the equatorial thermocline might be further enhanced. Observations ([Zhang et al. 1998](#)) suggest the potential that temperature (or thermocline depth) anomalies may propagate from subtropics to the Tropics with potential interior pathways, and on these 3–5 year timescales.

Further investigations will consider the role of interannual variability in mediating subtropical–tropical exchange, and the potential impact of the interior pathway on the equatorial circulation.

Acknowledgments

We are grateful to the TAO Project Office at PMEL for providing TAO mooring data for comparison with the model fields, to Drs. Rainer Bleck and Shan Sun for assistance with MICOM, and Dr. Paul Schopf for assistance with Poseidon. Discussions with Drs. Bill Dewar and David Adamec, and comments from Drs. Greg Johnson, Mike McPhaden, and two anonymous reviewers are gratefully acknowledged and helped to improve the manuscript. This study is a contribution to the NASA Seasonal to Interannual Prediction Project, which is funded as RTOP 622-24-47 by NASA's Earth Science Enterprise Global Modeling and Analysis Program.

REFERENCES

- Adamec D., 1998: Modulation of the seasonal cycle of the Kuroshio Extension during 1994 from satellite data. *J. Geophys. Res.*, **103**, 10209–10222. [Find this article online](#)
- Balmaseda M. A., M. K. Davey, and D. L. T. Anderson, 1995: Decadal and seasonal dependence of ENSO prediction skill. *J. Climate*, **8**, 2705–2715. [Find this article online](#)
- Baturin N. G., and P. P. Niiler, 1997: Effects of instability waves in the mixed layer of the equatorial Pacific. *J. Geophys. Res.*, **102**, 27771–27793. [Find this article online](#)
- Bleck R., and L. T. Smith, 1990: A wind-driven isopycnic coordinate model of the North and Equatorial Atlantic Ocean. 1: Model development and supporting experiments. *J. Geophys. Res.*, **95**, 3273–3285. [Find this article online](#)
- Bleck R., H. P. Hanson, D. Hu, and E. B. Kraus, 1989: Mixed layer–thermocline interaction in a three-dimensional isopycnic coordinate model. *J. Phys. Oceanogr.*, **19**, 1417–1439. [Find this article online](#)
- Bleck R., C. Rooth, D. Hu, and L. T. Smith, 1992: Salinity-driven transients in a wind- and thermohaline-forced isopycnic coordinate model of the North Atlantic. *J. Phys. Oceanogr.*, **22**, 1486–1505. [Find this article online](#)
- Butt J., and E. Lindstrom, 1994: Currents off the east coast of New Ireland, Papua New Guinea, and their relevance to regional undercurrents in the western equatorial Pacific Ocean. *J. Geophys. Res.*, **99**, 12503–12514. [Find this article online](#)
- Casey K. S., and P. Cornillon, 1999: A comparison of satellite and in situ based sea surface temperature climatologies. *J. Climate*, **12**, 1848–1863. [Find this article online](#)

- Chen D., S. E. Zebiak, M. A. Cane, and A. Busalacchi, 1997: Initialization and predictability of a coupled ENSO forecast model. *Mon. Wea. Rev.*, **125**, 773–788. [Find this article online](#)
- daSilva A. M., C. C. Young, and S. Levitus, 1994: *Atlas of Surface Marine Data 1994*. Vol. 1: *Algorithms and Procedures*, Tech. Rep., NOAA/National Oceanographic Data Center, 74 pp.
- Donguy J.-R., and G. Meyers, 1996: Mean annual variation of transport of major currents in the tropical Pacific Ocean. *Deep-Sea Res.*, **43**, 1105–1122. [Find this article online](#)
- Fine R. A., W. H. Peterson, and H. G. Ostlund, 1987: The penetration of tritium into the tropical Pacific. *J. Phys. Oceanogr.*, **17**, 553–564. [Find this article online](#)
- Gu D., and S. Philander, 1997: Interdecadal climate fluctuations that depend on exchanges between the Tropics and extratropics. *Science*, **275**, 805–807. [Find this article online](#)
- Hirst A., D. R. Jackett, and T. J. McDougall, 1996: The meridional overturning cells of a World Ocean model in neutral density coordinates. *J. Phys. Oceanogr.*, **26**, 775–791. [Find this article online](#)
- Huang B., and Z. Liu, 1999: Pacific subtropical–tropical thermocline water exchange in the National Centers for Environmental Prediction ocean model. *J. Geophys. Res.*, **104**, 11065–11076. [Find this article online](#)
- Johnson G. C., and M. J. McPhaden, 1999: Interior pycnocline flow from the subtropical to the equatorial Pacific Ocean. *J. Phys. Oceanogr.*, **29**, 3073–3089. [Find this article online](#)
- Kessler W. S., 1990: Observations of long Rossby waves in the northern tropical Pacific. *J. Geophys. Res.*, **95**, 5183–5217. [Find this article online](#)
- Kleeman R., J. P. McCreary, and B. A. Klinger, 1999: A mechanism for generating ENSO decadal variability. *Geophys. Res. Lett.*, **26**, 1743–1746. [Find this article online](#)
- Kraus E. B., and J. S. Turner, 1967: A one-dimensional model of the seasonal thermocline. II: The general theory and its consequences. *Tellus*, **19**, 98–106. [Find this article online](#)
- Legeckis R., 1977: Long waves in the eastern equatorial Pacific Ocean: A view from a geostationary satellite. *Science*, **197**, 1179–1181. [Find this article online](#)
- Levitus S., and T. Boyer, 1994: *World Ocean Atlas 1994*. Vol. 4: *Salinity*, NOAA Atlas NESDIS 3, U.S. Govt. Printing Office, 117 pp.
- Liu Z., and B. Huang, 1998: Why is there a tritium maximum in the central equatorial Pacific thermocline? *J. Phys. Oceanogr.*, **28**, 1527–1533. [Find this article online](#)
- Liu Z., and R.-H. Zhang, 1999: Propagation and mechanism of decadal upper-ocean variability in the North Pacific. *Geophys. Res. Lett.*, **26**, 739–742. [Find this article online](#)
- Lu P., and J. P. McCreary, 1995: Influence of the ITCZ on the flow of thermocline water from the subtropical to the equatorial Pacific Ocean. *J. Phys. Oceanogr.*, **25**, 3076–3088. [Find this article online](#)
- Lu P., J. P. McCreary, and B. A. Klinger, 1998: Meridional circulation cells and the source waters of the Pacific Equatorial Undercurrent. *J. Phys. Oceanogr.*, **28**, 62–84. [Find this article online](#)
- McCreary J. P., and P. Lu, 1994: Interaction between the subtropical and equatorial ocean circulations: The subtropical cell. *J. Phys. Oceanogr.*, **24**, 466–497. [Find this article online](#)
- McPhaden M. J., and R. A. Fine, 1988: A dynamical interpretation of the tritium maximum in the central equatorial Pacific. *J. Phys. Oceanogr.*, **18**, 1454–1457. [Find this article online](#)
- McPhaden M. J., Coauthors, 1998: The tropical ocean global atmosphere observing system: A decade of progress. *J. Geophys. Res.*, **103**, 14169–14240. [Find this article online](#)
- Meyers G., 1980: Do Sverdrup transports account for the Pacific North Equatorial Countercurrent? *J. Geophys. Res.*, **85**, 1073–1075. [Find this article online](#)
- Pacanowski R., and S. G. H. Philander, 1981: Parameterization of vertical mixing in numerical models of the tropical oceans. *J. Phys. Oceanogr.*, **11**, 1443–1451. [Find this article online](#)
- Reverdin G., C. Frankignoul, E. Kestenare, and M. J. McPhaden, 1994: Seasonal variability in the surface currents of the equatorial Pacific. *J. Geophys. Res.*, **99**, 20323–20343. [Find this article online](#)

- Rothstein L. M., R.-H. Zhang, A. J. Busalacchi, and D. Chen, 1998: A numerical simulation of the mean water pathways in the subtropical and tropical Pacific Ocean. *J. Phys. Oceanogr*, **28**, 322–343. [Find this article online](#)
- Schopf P. S., and A. Loughe, 1995: A reduced-gravity isopycnal ocean model: Hindcasts of El Niño. *Mon. Wea. Rev.*, **123**, 2839–2863. [Find this article online](#)
- Seager R., M. B. Blumenthal, and Y. Kushnir, 1995: An advective atmospheric mixed layer model for ocean modeling purposes: Global simulation of surface heat fluxes. *J. Climate*, **8**, 1951–1964. [Find this article online](#)
- Shapiro R., 1970: Smoothing, filtering and boundary effects. *Rev. Geophys. Space Phys*, **8**, 359–387. [Find this article online](#)
- Smagorinsky J. S., 1963: General circulation experiments with the primitive equations. I: The basic experiment. *Mon. Wea. Rev.*, **91**, 99–164. [Find this article online](#)
- Smith L. T., D. B. Boudra, and R. Bleck, 1990: A wind-driven isopycnic coordinate model of the north and equatorial Atlantic Ocean 2. The Atlantic Basin experiments. *J. Geophys. Res.*, **95**, 13105–13128. [Find this article online](#)
- Stricherz J., J. J. O'Brien, and D. M. Legler, 1992: *Atlas of Florida State University Tropical Pacific Winds for TOGA 1966–1985*. The Florida State University, 250 pp.
- Talley L. D., 1988: Potential vorticity distribution in the North Pacific. *J. Phys. Oceanogr*, **18**, 89–106. [Find this article online](#)
- Wang B., 1995: Interdecadal changes in El Niño onset in the last four decades. *J. Climate*, **8**, 267–285. [Find this article online](#)
- Wang B., R. Wu, and R. Lukas, 2000: Annual adjustment of the thermocline in the tropical Pacific Ocean. *J. Climate*, **13**, 596–616. [Find this article online](#)
- Weisberg R. H., and L. Qiao, 2000: Equatorial upwelling in the Central Pacific estimated from moored velocity profilers. *J. Phys. Oceanogr*, **30**, 105–124. [Find this article online](#)
- White W. B., 1974: The maintenance of the Pacific North Equatorial Countercurrent by thermal/mixing processes. *Deep-Sea Res.*, **21**, 347–358. [Find this article online](#)
- Wijffels S. E., 1993: Exchanges between gyres and hemispheres: A direct approach to the mean circulation of the equatorial Pacific Ocean. Ph.D. thesis, MIT–WHOI Joint Program in Oceanography, 294 pp.
- Wijffels S. E., J. M. Toole, H. L. Bryden, R. A. Fine, W. J. Jenkins, and J. L. Bullister, 1996: The water masses and circulation at 10°N in the Pacific. *Deep-Sea Res.*, **43**, 501–544. [Find this article online](#)
- Wyrski K., and B. Kilonsky, 1984: Mean water and current structure during the Hawaii-to-Tahiti Shuttle Experiment. *J. Phys. Oceanogr*, **14**, 242–254. [Find this article online](#)
- Xie P.-P., and P. A. Arkin, 1996: Analyses of global monthly precipitation using gauge observations, satellite estimates, and numerical model predictions. *J. Climate*, **9**, 840–858. [Find this article online](#)
- Yang S., K.-M. Lau, and P. S. Schopf, 1999: Sensitivity of the tropical Pacific Ocean to precipitation-induced freshwater flux. *Climate Dyn.*, **15**, 737–750. [Find this article online](#)
- Yu X., and M. J. McPhaden, 1999: Seasonal variability in the equatorial Pacific. *J. Phys. Oceanogr*, **29**, 925–947. [Find this article online](#)
- Yu Z., and P. S. Schopf, 1997: Vertical eddy mixing in the tropical upper ocean: Its influence on zonal currents. *J. Phys. Oceanogr*, **27**, 1447–1458. [Find this article online](#)
- Zhang R.-H., L. Rothstein, and A. Busalacchi, 1998: Origin of upper-ocean warming and El Niño change on decadal scales in the tropical Pacific Ocean. *Nature*, **391**, 879–883. [Find this article online](#)
- Zhang R.-H., L. Rothstein, A. Busalacchi, and X.-Z. Liang, 1999: The onset of the 1991–92 El Niño event in the tropical Pacific Ocean: The NECC subsurface pathway. *Geophys. Res. Lett.*, **26**, 847–850. [Find this article online](#)
- Zhang Y., J. M. Wallace, and D. Battisti, 1997: Enso-like interdecadal variability: 1900–93. *J. Climate*, **10**, 1004–1020. [Find this article online](#)

TABLE 1. Forcing datasets used to force the model simulations, and the mixing coefficients used

	MICOM	Poseidon
	Forcing set	
Shortwave radiation	COADS-delta (1994)	ERBE ^a
Precipitation	Xie and Arkin (1996)	Xie and Arkin (1996)
Wind and wind stress	FR-NCEP	FR-NCEP
Latent and sensible heat	Seager et al. (1995)	Seager et al. (1995)
Humidity	NCEP reanalysis	NCEP reanalysis
Air temperature	NCEP reanalysis	NCEP reanalysis
Cloud cover	ISCCP clim.	ISCCP clim.
Southern boundary	Levitus (1994)	Levitus (1994)
	Parameter set	
Isopycnal property mixing	$3 \times 10^6 \text{ m}^2 \text{ s}^{-1}$	Shapiro
Isopycnal isocentrism mixing	$7 \times 10^6 \text{ m}^2 \text{ s}^{-1}$	Shapiro
Diapycnal property mixing	$3 \times 10^{-10} \text{ m}^2 \text{ s}^{-1} (\text{N})$	Peszewski and Philander (1981)

Click on thumbnail for full-sized image.

TABLE 2. Volume transports (Sv) from observational sources and the models. Negative transports indicate southward or westward flow. NICU: New Ireland Coastal Undercurrent, NGCUC: New Guinea Coastal Undercurrent

Current	Observations	MICOM	Poseidon
NEC 155°W ^a	-23.3	-18.0	-16.5
NEC 155°W ^f	-15.3	-18.5	-20
NECC 155°W ^a	28.7	19.0	23.0
NECC 155°W ^f	14.2	21.0	17.0
NECC 165°E ^b	27.4	24.0	22.0
SEC 155°W ^a	-41.6	-37.0	-40.0
SEC 155°W ^f	-30.2	-31.5	-38.0
SEC 165°E ^b	-38.8 ± 17.5	-24.0	-32.0
EUC 155°W ^a	22.8	29.0	36.5
EUC 165°E ^b	19.7 ± 7.3	20.0	29.5
NICU 4°S ^c	5?	7.0	12.0
NGCUC 4°S ^c	7 ± 1.2	8.5	7.5
MC 12°N ^d	-16	-8.0	-21.0
MC 8°N ^d	-22	-23.0	-30.5
MC 8°N ^e	-24	-24.0	-32.0
MC 7°N ^d	-26	-26.0	-34.0
MC 5.5°N ^d	-33	-24.0	-28.0

^a From Wyrki and Kilonsky (1984). The SEC is their SEC from 9°S to 4°N, the NECC transport includes their NECC and NSCC. Model transports are above 400-m depth.

^b From Delcroix et al. (1987). The NECC includes his NEC and NSCC above 400 m.

^c From Butt and Lindstrom (1994). The NICU here includes all subsurface northward transport away from the western boundary current, as the New Ireland coastline is not resolved in the models. The estimate of observed transport comes from their schematic Fig. 7.

^d From Lukas et al. (1991). Their direct estimate from ADCP measurements is compared to model flow west of 130°E and above 300 m.

^e From Wijffels (1993). Her ADCP-corrected geostrophic estimates for transport above σ_θ of 26.7 kg m⁻³ are shown here. The model estimates are computed east of 130°E, for layers with σ_θ less than 26.7 kg m⁻³.

^f From Donguy and Meyers (1996). SEC transport to 20°S; and NEC transport north to 20°N.

Click on thumbnail for full-sized image.

TABLE 3. Seasonal volume transports (Sv) from observational sources and the models. The model transports were computed as closely as possible following the methods of the observations, and negative transports indicate southward or westward flow. No attempt was made to interpolate the model onto a finer vertical resolution, if a density layer missed one of the criteria, its transport was excluded

Current	Observations		MICOM		Poseidon	
	Max	Min	Max	Min	Max	Min
NECC 155°W	25	-25	29	-29	27	-27
NECC 155°W	16	-16	16	-16	16	-16
NECC 155°W	5	-5	9	-9	9	-9
NECC 155°W	13	-13	26	-26	22	-22
SEC 155°W	-36	36	-57	57	-60	60
SEC 155°W	-36	36	-47	47	-55	55
SEC 155°W	-20	20	-18	18	-16	16
SEC 155°W	-20	20	-31	31	-31	31
EUC 165°E	25	-25	35	-35	27	-27
EUC 165°E	14	-14	10	-10	22	-22
EUC 140°W	43	-43	43	-43	51	-51
EUC 140°W	29	-29	29	-29	24	-24
EUC 140°W	20	-20	20	-20	20	-20
EUC 140°W	16	-16	16	-16	27	-27

¹ From Donguy and Meyers (1996). SEC transport only to 10°S, the models show two minima and maxima. The models EUC transport is shown as seasonal average values.

² From Delcroix et al. (1987).

³ Estimated from Yu and McPhaden (1999) at 140°W. The model results are from 155°W, and show secondary maxima and minima.

Click on thumbnail for full-sized image.

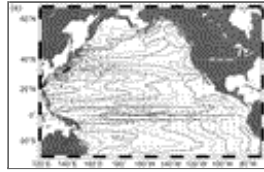
TABLE 4. Comparison of a 3-yr average of the models' transport (Sv) with other observations and models. The first column gives the name of the dataset for comparison, and the criteria used to delineate transport layers. JMcP: comparison of Johnson and McPhaden (1999), W1: transport calculation of Wijffels (1993), W2: transport calculation of Wijffels (1995), and HL: transport calculations from the NCEP model, described in Huang and Liu (1999)

Dataset	Criteria	Observations	MICOM	Poseidon
JMcP	W1	25	29	27
JMcP	W2	16	16	16
JMcP	HL	5	9	9
JMcP	HL	13	26	22
W1	W1	-36	-57	-60
W2	W2	-36	-47	-55
HL	HL	-20	-18	-16
HL	HL	-20	-31	-31
EUC	W1	25	35	27
EUC	W2	14	10	22
EUC	HL	43	43	51
EUC	HL	29	29	24
EUC	HL	20	20	20
EUC	HL	16	16	27

23.0–24.5	-2	-2.5	-8.5
24.5–26.2	-1	0	1.5
Total	-4	-4.5	-8.5
W2 at 8°N, W. Bdry–130°W σ_θ bounds:			
Surface–26.7	-24	-36	-23

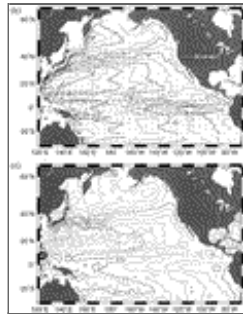
Click on thumbnail for full-sized image.

Figures



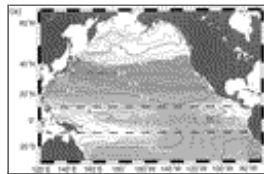
Click on thumbnail for full-sized image.

FIG. 1. Modeled and observed sea surface height fields in September. (a) MICOM SSH (cm), overlain by the mixed layer velocity field filtered onto 2° resolution. (b) Poseidon dynamic height field (J kg^{-1}) relative to 2200 m, overlain by mixed layer velocities. (c) Topex altimeter SSH field for Sep 1996 added to an annual Levitus climatological SSH field ([Adamec 1998](#))



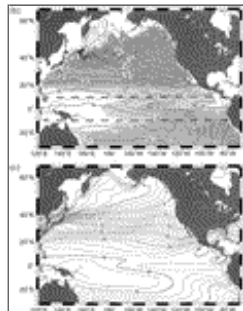
Click on thumbnail for full-sized image.

FIG. 1. (Continued)



Click on thumbnail for full-sized image.

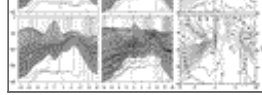
FIG. 2. Modeled and observed surface temperature ($^\circ\text{C}$) fields in March overlying surface density distributions. The surface density field is shaded where three thermocline layers [$\sigma_\theta = 20.0\text{--}23.0$ (light gray), $23.0\text{--}24.5$ (medium gray), $24.5\text{--}26.2$ (dark gray) kg m^{-3}] outcrop into the mixed layer. Heavy dashed lines indicate 10°N and S. (a) MICOM. (b) Poseidon. (c) Observed climatology from [Casey and Cornillon \(1999\)](#)



Click on thumbnail for full-sized image.

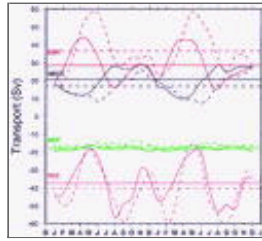
FIG. 2. (Continued)





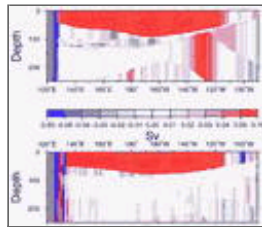
[Click on thumbnail for full-sized image.](#)

FIG. 3. Meridional sections of zonal velocity (contoured at 5 cm s^{-1} intervals), temperature (1°C intervals), and salinity (0.1 psu intervals) from the observations of [Wyrski and Kilonsky \(1984\)](#) and from an annual average of the last year of the model fields. The models' mean interface depths are represented by dots in the lowest panel, and three layers within the thermocline delineated by density ranges as in the text are shaded. (a: left column) MICOM. (b: middle column) Poseidon. (c: right column) Observations



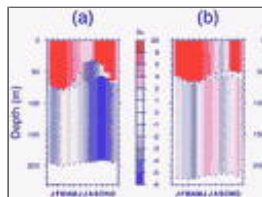
[Click on thumbnail for full-sized image.](#)

FIG. 4. Zonal mass transport (Sv) across 155°W according to the water mass definitions of [Wyrski and Kilonsky \(1984\)](#). (All transports above 400 m .) EUC: eastward flow between 2°N and S . NEC: westward flow between 8° and 18°N . NECC: eastward flow between 2° and 12°N . SEC: westward flow between 8°S and 5°N . Solid lines are for the MICOM model run, dashed lines are for Poseidon, and horizontal lines are the annual means



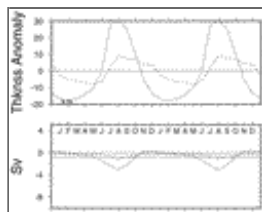
[Click on thumbnail for full-sized image.](#)

FIG. 5. Meridional volume transport (Sv) across 10°N averaged over the 3-yr climatology within layers. Red indicates average northward flow, and blue southward flow. The upper panel is the MICOM simulation, the lower panel is Poseidon



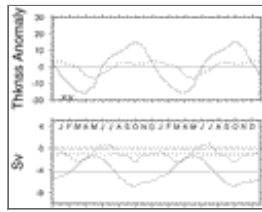
[Click on thumbnail for full-sized image.](#)

FIG. 6. Meridional volume transport integrated zonally across the basin interior from 160°E eastward within density layers at 8°N ($\sigma_\theta = 22.0\text{--}23.0, 23.0\text{--}26.2 \text{ kg m}^{-3}$) is shown over an annual cycle. The net layer transport is shown over the average layer thickness to suggest the vertical structure of the meridional flow. Blue shades indicate southward transport, and red shades are northward transport. (a) MICOM simulation and (b) Poseidon simulation



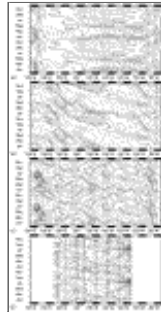
[Click on thumbnail for full-sized image.](#)

FIG. 7. Thickness anomaly of the upper thermocline layer at 8°N averaged zonally across the basin between 170°E and 130°W . Positive thickness anomalies reflect a thickening of the layer, and corresponding southward transport. (bottom) Meridional transport integrated across the basin at 8°N between 170°E and 130°W within the upper thermocline layer. The solid line is for MICOM simulations, the dashed line is for Poseidon, and horizontal lines indicate annual means



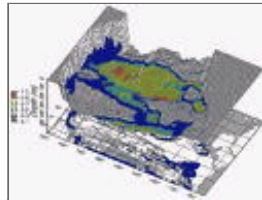
Click on thumbnail for full-sized image.

FIG. 8. As in Fig. 7 but for the lower thermocline layers



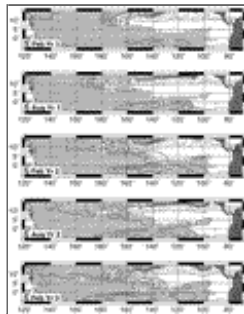
Click on thumbnail for full-sized image.

FIG. 9. (a) Hovmöller diagram of Ekman pumping at 8°N computed from the FSU climatological winds used to force the models ($\times 10^4 \text{ m s}^{-1}$). (b)–(d) Modeled and observed thermocline thickness anomalies delineated by the 24°C and 13°C isotherms. The contour interval for panels b, c, and d is 2.5 m. (b) MICOM. (c) Poseidon. (d) The data from the TOGA TAO moorings at 7°, 8°, and 9°N averaged onto an annual climatology. Circles represent data points



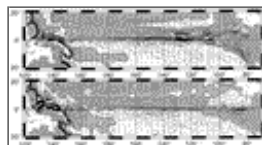
Click on thumbnail for full-sized image.

FIG. 10. The ideal ventilation tracer concentration for layer 10 ($\sigma_\theta = 25.0$) in Feb three winters after the initial tracer release is color shaded and overlays the surface representing depth of the base of this layer. The contour interval is 0.2 ideal tracer units, with a maximum initial condition of 1 (red) indicating a layer completely ventilated with mixed layer water. Contoured below is the thickness of the layer in meters



Click on thumbnail for full-sized image.

FIG. 11. The ideal ventilation tracer concentration for layer 10 ($\sigma_\theta = 25.0$). Shading indicates regions where this layer has thickness greater than 5 m. The uppermost panel is the second Feb (18 months) following the tracer release in Sep. The panels then show the tracer concentration every six months for 2.5 years, with time increasing downward



Click on thumbnail for full-sized image.

FIG. 12. Annually averaged meridional velocity within the lower thermocline contoured at 0.5 cm s^{-1} intervals. Southward flow is shaded, and annually averaged velocity vectors for the layer are superimposed. (top) MICOM layer 10 and (bottom) Poseidon layer 9

Corresponding author address: Dr. Victoria J. Coles, GEST, Code 971, NASA GSFC, Greenbelt, MD 20771. E-mail: vcoles@mohawk.gsfc.nasa.gov

top ▲



© 2008 American Meteorological Society [Privacy Policy and Disclaimer](#)
Headquarters: 45 Beacon Street Boston, MA 02108-3693
DC Office: 1120 G Street, NW, Suite 800 Washington DC, 20005-3826
amsinfo@ametsoc.org Phone: 617-227-2425 Fax: 617-742-8718
[Allen Press, Inc.](#) assists in the online publication of *AMS* journals.